Measurement of Ocean Wave Directional Spectra Using Doppler Side-Scan Sonar Arrays

MARK V. TREVORROW

Ocean Physics, Institute of Ocean Sciences, Sidney, British Columbia, Canada

(Manuscript received 1 March 1994, in final form 14 November 1994)

ABSTRACT

A technique is presented for extraction of ocean wave directional spectra using Doppler side-scan sonars. Two 103-kHz steerable side-scan beams from a freely drifting subsurface platform are used to estimate horizontal water surface velocity due to waves. The side-scan targets are clouds or layers of microscopic air bubbles, confined to within a few meters of the ocean surface. Upward-looking sonars are used to estimate the surface height power spectrum. The side-scans are steered to compensate for any platform yaw, and corrections to the measured wave velocity due to horizontal and vertical platform motion must be applied. Measurements of wave velocity with the side-scans in this geometry are found to have acceptable spectral signal-to-noise properties at horizontal ranges up to 150 m in the frequency range 0.05–0.35 Hz, with degraded performance at greater range. Time series of horizontal wave velocity at 16 range points along each of two orthogonal beams are used in a maximum-likelihood array processing technique to estimate the directional spreading functions versus frequency. Numerical and experimental tests suggest that the maximum-likelihood method can reconstruct adequately unimodal and bimodal wave fields. These methods are demonstrated with ocean data from the northeastern Pacific.

1. Introduction

The measurement of surface wave frequency–directional spectra in the open ocean is a challenging oceanographic problem. In shallow water it is convenient to use spatially distributed arrays of wave gauges, pressure sensors, or current meters. These are generally fixed to the seabed or mounted on rigid platforms (e.g., Pawka 1983; Herbers and Guza 1990; Herbers et al. 1991; Donelan et al. 1985). Large arrays of wave gauges are more difficult to implement in the open ocean due to the lack of any fixed reference point or any physical means of supporting a large aperture array. A common approach in the open ocean is to make single-point measurements of three (or more) wave properties (for example, a heave–pitch–roll buoy, cloverleaf buoy, or pressure–current meter combination). A great deal of literature exists on various direct and data-adaptive processing methods for buoy data (e.g., Longuet-Higgins et al. 1963; Long and Hasselmann 1979; Lygre and Krogstad 1986; Marsden and Juszko 1987; Oltman-Shay and Guza 1984). A useful summary of existing directional buoy technology is given by Allender et al. (1989). As surface floats these buoys are subject to damage from shipping, by extreme waves during storms, or by ice-coating under Arctic conditions. The directional performance of surface buoys can be moderately good using data-adaptive processing methods, but multielement spatial arrays have the potential for improved performance.

The past few years have seen the emergence of exciting new techniques for probing ocean surface processes using high-frequency underwater acoustics. Near-surface active acoustic methods take advantage of copious quantities of microscopic air bubbles injected by wave breaking. It has been found that the size of these microbubbles is limited to radii from roughly 10 to 200 μm with peak densities near a 20-μm radius (see Crawford and Farmer 1987; Farmer and Vagle 1989). Due to their small size, large acoustic target strength, and large numbers, these microbubbles serve as excellent tracers of water particle motion. Under typical open ocean conditions with winds more than 5 m s^{-1}, wave-breaking activity is sufficient to create layers or plumes of microbubbles that serve as excellent side-scan targets. There is a readily measurable acoustic Doppler shift in the side-scan echoes due to the large orbital velocities induced by surface waves. This horizontal Doppler velocity has been previously used to investigate surface waves (Krogstad et al. 1988; Pinkel and Smith 1987; Smith 1989; Herbers et al. 1991) and is the focus of this paper. Very recent work by Smith and Bullard (1995) presents an alternate technique for extraction of the wave directional spectrum from Doppler sonar data and gives a more-detailed investigation of wave measurement problems.

Corresponding author address: Dr. Mark V. Trevorrow, Ocean Physics, Institute of Ocean Sciences, P.O. Box 6000, 9860 West Saanich Road, Sidney, BC V8L 4B2, Canada.

Here, two 360° steerable side-scans and several vertical sonars are used, mounted on a freely drifting, self-contained platform at an approximate 25-m depth. The side-scans are oriented orthogonally and steered to compensate for platform yaw, yielding radial velocity versus range, which can be treated similarly to a two-dimensional array of current meters. Corrections for measurement geometry and horizontal and vertical platform motions must be applied. This array geometry, in combination with the *radial* character of the side-scan velocity measurements, is less than optimal for directional spectrum calculations. Additionally, considerable velocity spectral *noise* due to natural bubble-cloud variability limits measurements to less than 0.35 Hz at ranges up to 150 m. Still, useful directional spectra can be extracted, which in combination with vertical sonar and side-scan intensity images yield a valuable suite of data. Maximum-likelihood (ML) cross-spectral array processing algorithms are used to extract the directional spreading functions versus frequency. The ML directional estimation method was chosen for its simplicity and robustness in the presence of noisy cross-spectral data. Vertical sonars simultaneously yield a direct and accurate determination of the sea surface elevation, from which wave height spectra can be derived (Zedel 1994).

The next section summarizes techniques used to measure Doppler velocity due to waves in the open ocean and discusses some of the characteristics and limitations of these measurements. The following sections describe techniques for extracting the directional spectrum and some numerical tests using synthetically generated wave fields. Finally, results from an open ocean test in the northeastern Pacific during December 1993 will be presented.

2. Doppler velocity measurements in ocean waves

Over the past few years the acoustics group at the Institute of Ocean Sciences has developed several autonomous underwater acoustics platforms, of which SeaScan is the most recent. [See Trevorrow and Teichrob (1994) for a detailed description.] This platform supports six upward-looking conical-beam sonars (29–397 kHz) and two outward-looking steerable side-scans (103 kHz). It is completely self-contained with sufficient battery and data recorders for 48 h of operation. Figure 1 shows a sketch of the platform deployment scheme and acoustic-beam geometry. The platform is suspended at a 20–30-m depth by a rubber bungy cord below a 1-m-diameter surface buoy. The rubber cord largely decouples the platform from surface buoy motions. The vertical sonars have beamwidths (to −3 dB) in the range ±1.5° to ±5°. The side-scans have *fan* beams with horizontal and vertical beamwidths of ±1.5° and ±25°, respectively. The main axis of each side-scan is elevated 15° above horizontal. The sonar and side-scan ping repetition rate is 1.667 Hz. The platform motions are measured by a magnetic flux gate compass, vertical accelerometer, and two-axis tiltmeter.

The basic data from each sonar or side-scan consist of sequences of quadrature-sampled echoes, forming a complex time series sampled at 7350 Hz. A 4.35-ms phase-encoded pulse is transmitted by the two 103-kHz side scans. The side-scan echo is recorded for 390 ms, allowing a maximum horizontal range of 289 m. The Doppler velocity of the signal is then calculated within 3.2-m range bins, centered at 1.01-m range intervals, using standard time-domain complex covariance algorithms (e.g., Miller and Rochwarger 1972), modified for repeat-sequence Barker code pulses to decrease estimation variance (Smith and Pinkel 1991; Brumley et al. 1991; Pinkel and Smith 1992; Trevorrow and Farmer 1992). The SeaScan instrument uses 4.6 repetitions of a 7-bit code, with a bit length of 0.1361 ms, yielding a predicted velocity estimation uncertainty (square root of variance) of 14 cm s^{-1} and a velocity aliasing limit of ±3.8 m s^{-1}. The Doppler velocity versus range data contained occasional spikes (evident as abrupt jumps to the aliasing velocity limits), attributed to electronic noise within the instrument platform. These were removed by interpolating velocity from neighboring, unaffected range points. It is plausible that a small fraction of these spikes may have been induced by intense signal decorrelation under breaking waves, which is investigated in more detail by Smith and Bullard (1995). Apart from the spikes, the measured ve-

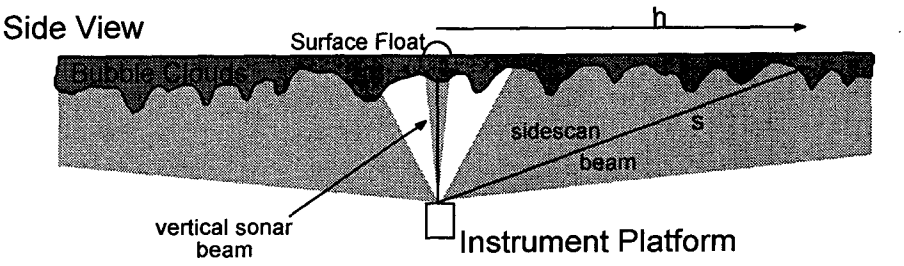

FIG. 1. Diagram of vertical sonar and steerable side-scan beam geometry. The acoustics platform is suspended at a 25-m (nominal) depth.

locities only rarely exceeded one-half of the aliasing limit, so aliasing effects were ignored.

The echo received by the sonars and side-scans will be the integration of scattering from microbubbles, the surface, and other particulates distributed within the insonified volume. However, under typical oceanic conditions with winds more than 5 m s^{-1}, plentiful microbubble scatterers are found within a few meters of the surface. Furthermore, the backscattering cross section of resonant microbubbles is many orders-of-magnitude stronger than for solid particles or for Bragg scattering from the surface. Thus, the side-scan echo (intensity and Doppler velocity) will be dominated completely by *near-surface* microbubble clouds and wave velocities. A near-surface scattering volume, bounded by the side-scan horizontal beam angle (±1.5°) and the pulse length (3.2 m), can be referenced to the horizontal distance h from a point directly above the platform. This is accomplished for each range bin at slant range s with a side-scan depth d using the simple Pythagorean formula $h = (s^2 - d^2)^{1/2}$. This implies a surface grazing angle $\phi(h) = \arctan(d/h)$, and corrections for a finite grazing angle at short range will need to be applied. At short range (<50 m), some small variations in h at fixed slant range will be induced by vertical platform displacement, so data where $h < d$ should be avoided (e.g., for worst case at d, h = 25 m, $\delta h = \delta d \approx$ 50 cm rms typical). The spectral phase error associated with this horizontal *jitter* is small [i.e., at worst for 0.35-Hz waves, $2\pi\delta h \times (\text{wavelength})^{-1} = 14°$]. This side-scan measurement geometry yields *radial* velocity, confined to the azimuthal heading of the side-scan beam.

The vertical sonars yield accurate measurements of the ocean surface elevation due to waves and volume scattering due to microbubble clouds beneath the surface. A typical acoustic image from the 118-kHz vertical sonar (Fig. 2) shows depth and time variations of natural microbubble plumes in the ocean. This 118-kHz sonar is predominantly sensitive to scattering from microbubbles with a radius of 28 μm. The sonar backscatter is referenced to the instantaneous surface height, the vertical resolution is 10 cm, and each horizontal pixel is an average of 10 pings. A small wind-induced drift current (~8 cm s^{-1}) moved the bubble plumes past the sonar beams. Through examination of data similar to Fig. 2, the acoustic target strength has been observed to decay roughly exponentially with depth z, that is, as $e^{z/l}$ ($z < 0$, positive upward), with e-folding scale l in the range of 0.4–1.5 m (Crawford and Farmer 1987; Thorpe 1982). The 12-s-averaged e-folding depth scale for data shown in Fig. 2 is in the range of 0.45–1.15 m, with a mean of 0.59 ± 0.12 m. Taking an arbitrary definition of the bubble-cloud depth as $5l$, which encompasses 99% of the acoustic backscatter, the typical bubble depth is about 3 m. This 3-m-thick

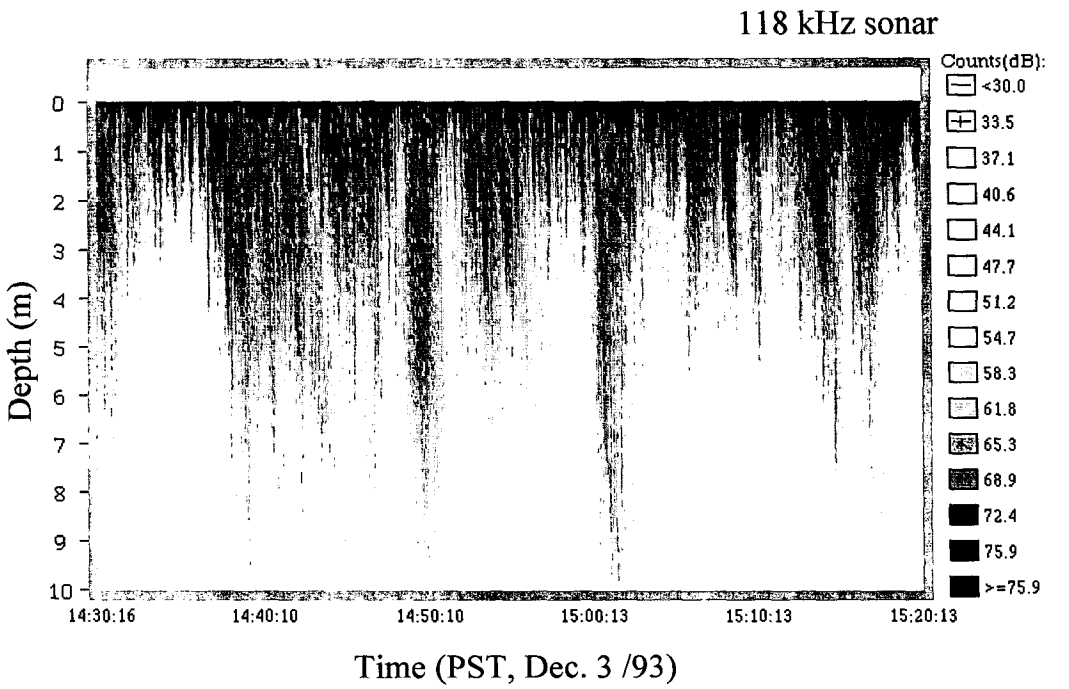

FIG. 2. The 118-kHz vertical sonar intensity (dB, arbitrary) vs depth and time from SeaScan, 3 December 1993 in northeastern Pacific. Each horizontal pixel is averaged over 6 s, with depth referenced to the instantaneous ocean surface height.

microbubble region provides the dominant targets for side-scan backscatter.

The volumetric backscatter from a side-scan is integrated in range over one pulse length and is a weighted depth integral depending on the vertical target strength variation. The wave velocity depth variation in deep water is $u(z) = u_0 e^{kz}$, where u_0 is the surface velocity and k is the wavenumber. Using a simple one-dimensional model, the depth-integrated velocity $\bar{u}$, weighted by acoustic target strength, can be evaluated as $\bar{u} = u_0(lk + 1)^{-1}$. For long-period swell waves, the product $lk \ll 1$, so the measured velocity equals the surface value, but the effect is more pronounced at higher frequencies. In our example with a maximum e-folding depth of 1.15 m, a 0.2-Hz wave will see a 16% velocity reduction, and a 0.3-Hz wave will be reduced by 29%. This velocity amplitude reduction, which is both spatially and temporally varying, increases the measurement uncertainty and distorts the velocity spectra. The vertical sonars, which are able to penetrate through the bubble cloud and measure the surface elevation directly, provide superior estimates of wave height spectra (see Zedel 1994).

This Doppler velocity estimation has a limited horizontal range. Dominantly, the side-scan echo strength decays roughly as s^{-2} along with intrinsic seawater absorption (0.032 dB m^{-1}), so that at longer ranges (>200 m) instrumental signal-to-noise limitations will be encountered. At shallow grazing angles (<6°), small-scale velocities found near the crests of steep waves will be lost by *shadowing* behind wave troughs. Additionally, there will be spatially and temporally varying attenuation by bubbles along the acoustic path, with rays penetrating nearer the surface and through dense bubble clouds, suffering greater attenuation. At larger range, echoes from deeper parts of the bubble plumes (with diminished high-frequency velocities) will be enhanced relative to echoes from the near surface. Smith (1989) and Smith and Bullard (1995) present a more-detailed discussion of these measurement problems. Also, with a ±1.5° horizontal beamwidth, the insonified volume has an increasing transverse dimension, which approaches 13 m at 250-m range.

The net effect of this velocity degradation with range is evident from the time-averaged velocity power and spatial cross-spectra along a side-scan beam, as shown in Fig. 3. These uncorrected spectra include effects of platform motion. In this case, a 6-m aperture (2 × pulse length), along-beam spatial coherence is representative of the cross-spectral data required for directional spectrum calculations. At ranges up to 100 m the velocity spectra are essentially identical. At a 100-m range, the power and coherence spectra reveal a velocity spectral floor of 0.06 $m^2\ s^{-2}\ Hz^{-1}$, evident at frequencies below 0.02 Hz and above 0.4 Hz. The decrease in coherence at frequencies above 0.3 Hz in the 100-m spectrum is

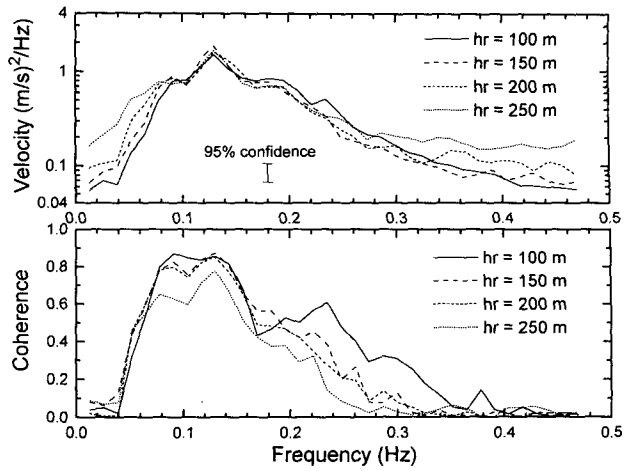

FIG. 3. Side-scan uncorrected velocity power spectra and spatial cross-spectral coherence (6 m along beam) at four horizontal ranges taken 3 December 1993 starting at 1430 PST. Spectra are derived from 128-point FFTs, 50% overlapped, averaged over 51 min at 0.6-s intervals.

physically reasonable for a directionally spread windsea with wavelengths comparable to the 6-m aperture. This spectral white noise floor corresponds to a mean-square velocity estimation variance of 0.05 $m^2\ s^{-2}$, which is 2.5 times the idealized 0.02 $m^2\ s^{-2}$ estimation variance predicted theoretically for this phase-encoded transmission (Pinkel and Smith 1992). At ranges of 150 m and beyond this noise floor increases, and higher-frequency components are progressively lost, such that at a 250-m range the noise spectral level approaches 0.16 $m^2\ s^2\ Hz^{-1}$, and spectral components above 0.23 Hz are lost in the noise.

Corrections for motion of the SeaScan platform must be made in the measured side-scan velocities. Figure 4 shows 5-min time series of platform motion parameters sampled every 0.6 s. Vertical displacement (Fig. 4e) was double integrated from the measured vertical acceleration and high-pass filtered at 0.04 Hz. The dynamic tilt of the platform (Fig. 4c) was roughly ±0.5°, which implies only negligible sonar or side-scan motion due to pitch and roll. The compass heading (Fig. 4d), with precision of ±0.1° and accuracy of ±0.5°, revealed a maximum platform yaw rate of close to 2° s^{-1}, which was well within the compass maximum yaw rate of 10° s^{-1}. The steerable side scans could accommodate a maximum step size of 2.813° per ping cycle, or 4.69° s^{-1}, so the yaw compensation kept up with platform rotation. The minimum side-scan step was 0.11°. Notice the long-period coherence between the sonar surface height and the vertical acceleration, indicating that SeaScan was moving in direct response to the orbital motion from long-period waves. In rough terms, a 12-s wave of amplitude 1.5 m would drive at a 22-m depth an orbital displacement of a 0.8-m ampli-

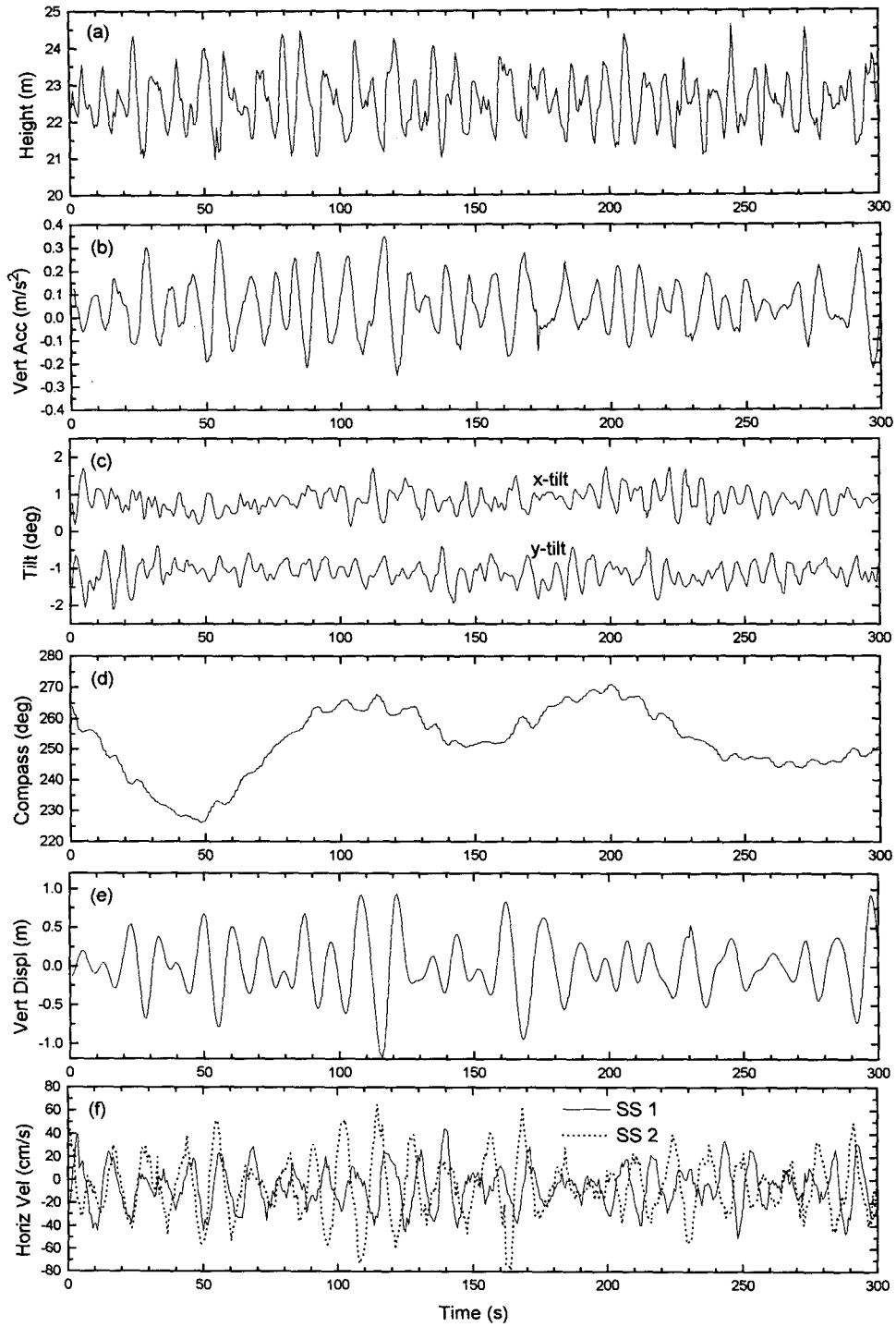

FIG. 4. Example of SeaScan platform motion parameters, taken at 1430 PST 3 December 1994: (a) raw surface height from sonars, (b) vertical acceleration, (c) x and y tilt, (d) compass heading, (e) vertical displacement (double-integrated acceleration), and (f) side-scan range-averaged (50–200 m) velocity.

tude, which agrees with the magnitude shown in Fig. 4e. At shorter ranges, the side-scan velocity measurements will be contaminated by vertical platform velocity, which can be removed at each range point by subtracting the integrated vertical acceleration, corrected for grazing angle. Note that this vertical motion

under wave forcing implies a coupled horizontal motion, which will contaminate the side-scan velocities. This is confirmed by a strong wave-period coherence between the vertical displacement and range-averaged Doppler velocity from SS 2 (Fig. 4f). This side-scan velocity was averaged from 50 to 200 m along each beam, corrected for grazing angle.

This range-averaged side-scan velocity is, thus, an indicator of horizontal platform motion in the side-scan beam direction. In the absence of direct horizontal motion measurements (i.e., from horizontal accelerometers), these range-averaged side-scan velocity components must be used. Unfortunately, range averaging over a 150-m aperture is seriously affected by long-period surface waves, requiring a scheme to remove long-period wave components. Assuming a single low-frequency wave component is present, a reference curve of the form $v_0 + A\cos(Bh + C)$ (where v_0, A, B, C are free parameters) can be fitted through the velocity versus horizontal range curve from each side-scan ping using an iterative least-squares approach. The v_0 term yields a largely unbiased estimate of the horizontal platform velocity component along each side-scan beam, which can be removed. Figure 5 shows an example velocity versus range curve and the fitted long-period reference. Time averaging of the mean horizontal velocity along each side-scan beam can be used to estimate the relative surface drift currents. At the time shown in Fig. 4, the 5-min mean current was 8.0 cm s^{-1} toward 199°.

The six vertical sonars transmit a short 0.5-ms ping that is used for volume scattering and surface elevation measurements. Zedel (1994) summarizes techniques for surface elevation measurement using a vertically oriented sonar. The surface is identified as the largest positive first derivative of echo amplitude versus range. Surface heights from the three highest-frequency sonars (118, 198, 397 kHz) are averaged together to yield an estimate with resolution ±3 cm. The wave height spectrum is then calculated from 40 to 50 averages of 128-point FFT (fast Fourier transform) variance-normalized spectra (50% overlapped, de-meaned, cosine-squared window). The vertical accelerometer signal, high-pass filtered at 0.04 Hz and double integrated, is used to compensate for the vertical displacement of the instrument platform. At much higher wind speeds there exists the potential for shadowing of the surface by dense, subsurface bubble clouds—especially at frequencies between roughly 5 and 50 kHz. This problem was not encountered in the analysis of the present data, using 118-, 198-, 397-kHz sonars. Overall, the measured wave height spectral noise levels were less than about 0.005 m^2 Hz^{-1}.

One subtlety with this surface height measurement is that the finite beamwidth of the sonars acts as a low-pass spatial filter, underestimating wave energy at frequencies above roughly 0.3 Hz. With an average ±3°

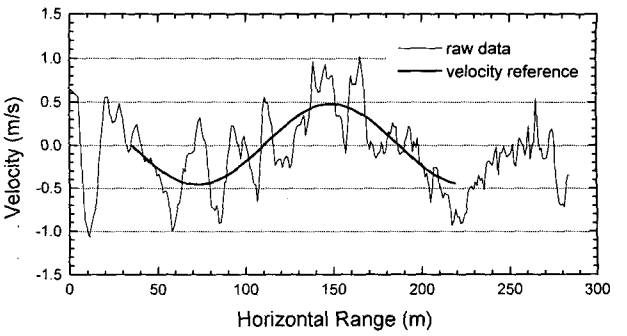

FIG. 5. Side-scan velocity vs horizontal range (single ping) near 1430 PST 3 December 1993, with fitted long-period wave velocity, $0.011 + 0.469\cos(0.0413h + 0.134)$ m s^{-1}, where h is range in meters.

beamwidth and a depth of 25 m, the surface footprint of the sonar beams is a circle of 2.6-m diameter. A spectral transfer function quantifying this spatial filtering effect can be calculated by comparing the variance of reference and spatially filtered single-frequency time series. For example, at 0.35 Hz (λ = 12.7 m) the variance reduction factor is 0.716. This variance reduction is negligible at low frequencies and rapidly increases at frequencies above about 0.3 Hz. The wave height spectra shown herein are corrected using these variance ratios. The spectra are truncated at frequencies above $\lambda = 2 \times$ footprint diameter, which for our geometry corresponds to roughly 0.50 Hz.

3. Extraction of directional spectrum

The directional spectrum of ocean surface gravity waves describes the frequency and azimuthal distribution of wave power and is denoted herein as $G(\omega, \theta)$, where ω is the frequency (rad s^{-1} or Hz) and θ is the azimuthal angle (radians or degrees) that the waves propagate *toward*. (This definition will be used throughout.) The units of $G(\omega, \theta)$ are square meters per hertz per radian. We can separate the directional spectrum into two components,

$$G(\omega, \theta) = D(\omega, \theta)S(\omega), \qquad (1)$$

where $D(\omega, \theta)$ is the directional spreading function, containing information on the spread of wave energy at each frequency, and $S(\omega)$ is the one-dimensional wave height spectrum, containing information on the total wave power at each frequency. The directional spreading functions are normalized so that

$$\int_0^{2\pi} D(\omega, \theta)\, d\theta = 1 \qquad (2)$$

for each frequency. This separation is convenient as we need only focus on calculation of $D(\omega, \theta)$. The one-dimensional wave height spectrum $S(\omega)$ is calculated from the vertical sonars, as previously explained. This

implies that absolute amplitude information need not be carried through the calculation of $D(\omega, \theta)$, because it will be normalized at the last stage.

In all of the following analysis we shall assume deep-water linear water wave dispersion and particle motion and ignore any effects of surface currents. However, this method could be easily adapted to shallow-water or nonlinear wave descriptions. The dispersion relation between angular frequency ω ($=2\pi f$, where f is the frequency in hertz) and wavenumber k ($=2\pi/\lambda$, where λ is the wavelength) is

$$\omega^2 = gk \quad \text{or} \quad \lambda = \frac{g}{2\pi f^2}, \tag{3}$$

where g is the acceleration due to gravity (9.805 m s^{-2}). Also, the spectral transfer function between surface elevation $\eta(f)$ and horizontal water particle velocity at depth $zu(f, z)$ is simply

$$u(f, z) = 2\pi f e^{kz}\eta(f) \quad (z < 0, \quad \text{positive up}). \tag{4}$$

A simplifying assumption that the microbubble scatterers lie at or near the surface will also be used, within caveats as discussed above.

This method uses the two side-scan beams pointed perpendicular to each other in a geometry fixed to a particular compass heading (i.e., defining a horizontal x–y *earth-fixed* coordinate system). The beams need to be constantly steered to compensate for any azimuthal rotation of the instrument platform. Unfortunately, for the purpose of directional spectrum calculations, this array geometry is suboptimal. One reason for this is the avoidance of short-range, high-grazing angle ($h < d$) data, which makes the spatial lags between the two array axes large. Also, the *radial* character of the measured side-scan velocity makes the data effectively blind to waves traveling perpendicular to that side-scan beam. Within these geometric limitations, however, a conventional ML array processing scheme can be formulated to extract the directional spreading functions with reasonable fidelity. The ML algorithm described here follows with only minor modifications from work done with a platform-mounted sonar system in the North Sea by Krogstad et al. (1988), which in turn was derived from well-known array directional spectral methods (e.g., Davis and Regier 1977; Pawka 1983).

We define the side-scan 1 beam as the x axis, with horizontal measurement points at distances x_j, $j = 1, 2, \cdots, N$, and side-scan 2 as the y axis, with measurement points at distances y_j, $j = N + 1, \cdots, 2N$. The basic data for the ML method is the ensemble-averaged, normalized horizontal velocity cross-spectral matrix $\Phi(\omega)$ ($2N \times 2N$, complex), derived from the cross-spectrum $\phi_{jk}(\omega)$ between any two measurement locations $\mathbf{x}$ and $\mathbf{x}_k$. This is related to the wave field via (suppressing the ω dependence and using matrix notation)

$$\Phi = \left[\frac{\phi_{jk}}{R_j R_k^* S}\right] = \int_0^{2\pi} \Pi \cdot \Pi^{*\mathrm{T}} D(\theta) d\theta, \tag{5}$$

where $R(\omega)$ is the velocity to surface elevation transfer function, the superscript *T denotes conjugate transpose, and $\Pi(\theta)$ is a geometry vector of the form ($2N \times 1$, complex)

$$\Pi(\theta) = \begin{bmatrix} \cos\theta e^{ikx_1\cos\theta} \\ \vdots \\ \cos\theta e^{ikx_N\cos\theta} \\ \sin\theta e^{iky_{N+1}\sin\theta} \\ \vdots \\ \sin\theta e^{iky_{2N}\sin\theta} \end{bmatrix}. \tag{6}$$

Note that Eqs. (5) and (6) provide a method to calculate directly the cross-spectral matrix by integrating overall directions a given directional spread $D(\theta)$ and array geometry $\Pi(\theta)$. This will be used in an iterative scheme described below and for numerical testing. The ML solution to the integral in Eq. (5) is

$$\hat{D}(\theta) = \frac{K}{\Pi^{*\mathrm{T}}\Phi^{-1}\Pi}, \tag{7}$$

where K is a normalization constant and Φ^{-1} is the generalized inverse of the cross-spectral matrix. This solution is derived as a minimization problem for each wave propagation angle θ. All computations are done with angles defined in the mathematical sense (counterclockwise), then converted to compass headings (clockwise from North) for display. This equation is solved for 180 angles in a full circle (2° *numerical* resolution). Note that in this case Φ is square, complex Hermitian (i.e., $\Phi_{ij} = \Phi_{ji}^*$), and all measurement points are independent, so a true mathematical inverse does exist. Still, the matrix may be *numerically* singular and sensitive to noise, which makes calculating the matrix inverse a nontrivial matter. A complex LU (Choleskii) decomposition technique with partial pivoting and using double precision is used. Numerical tests suggest that making this matrix too large (i.e., increasing the number of measurement points) leads to numerical instabilities without increasing the angular resolution noticeably. Through numerical simulation of a variety of array spacings, reasonable performance was found for $N = 16$ measurement points along each beam, which are spaced every 6.1 m from 25 to 123 m in horizontal range. Note that it is possible to incorporate the sonar surface height information (a direct measurement of $\eta(t)$ at $x, y = 0$) into this ML cross-spectral matrix formulation. However, Krogstad et al. found no significant differences in the directional spectra by omitting this additional wave height measurement (in their case pressure), which was confirmed by similar tests in this context.

In general, the ML solution does not match the input cross-spectral matrix. The basic ML solution, denoted $\hat{D}(\theta)$, is typically a *smeared* version of the true $D(\theta)$, especially at low frequencies where the wavelengths greatly exceed the array aperture. An iterative scheme exists to improve the angular resolution of the standard ML method. Note that Eqs. (5)–(7) above form a nonlinear operator, mapping any given $D(\theta)$ to the maximum likelihood estimate. We shall denote this operator $M[D(\theta)]$. Some improvement in resolution can be obtained by applying an iterative correction (from Marsden and Juszko 1987)

$$D_{n+1}(\theta) = D_n(\theta) + \frac{|\chi|^{1+\epsilon} D_n(\theta)}{\psi\chi}, \tag{8}$$

with

$$\chi = 1 - \frac{M[D_n(\theta)]}{\hat{D}(\theta)}, \tag{9}$$

where ϵ and ψ are adjustable parameters that control convergence rates, with recommended values $\epsilon = 1$ and $\psi = 10$. This iterative ML (IML) calculation is continued for 10–20 iterations and typically converges to less than an approximate 0.1% change in the values of $D_n(\theta)$, depending on frequency, type of directional distribution, and data quality.

A small geometric correction must be made to remove the effects of nonzero side-scan grazing angle. The measured radial velocity at a given range will contain both horizontal (desired) and vertical velocity contributions depending on the grazing angle ϕ and wave propagation angle θ (w.r.t. the side-scan beam), that is, in the spectral domain

$$v_{\text{radial}}(\omega) = u(\omega)\cos\theta\cos\phi - iw(\omega)\sin\phi, \tag{10}$$

where u and w are the horizontal and vertical velocity spectral components, which for deep water waves are of equal magnitude. This correction is best applied to the array geometry vector [Eq. (6)] which when modified becomes

$$\Pi(\theta) = \begin{bmatrix} (\cos\theta\cos\phi_1 - i\sin\phi_1)e^{ikx_1\cos\theta} \\ \vdots \\ (\cos\theta\cos\phi_N - i\sin\phi_N)e^{ikx_N\cos\theta} \\ (\sin\theta\cos\phi_1 - i\sin\phi_1)e^{iky_{N+1}\sin\theta} \\ \vdots \\ (\sin\theta\cos\phi_N - i\sin\phi_N)e^{iky_{2N}\sin\theta} \end{bmatrix}. \tag{11}$$

As input to the ML and IML calculations, time series of velocity at each range point along the two beams, sampled once every 0.6 s, need be collected for approximately 50 min. Obviously, this spectral-averaging time needs to be as long as possible to improve spectral estimation accuracy but is limited by the constraints of wave field stationarity, and 40 or 50 × 128-ping sets appears to be a reasonable compromise. The time series are low-pass filtered to remove components above 0.4 Hz. Then frequency spectra are calculated at each measurement point and formed into separate cross-spectral matrices, one for each frequency. A 128-point FFT with 50% overlap and cosine-squared window is used, yielding a frequency spacing of 0.013 Hz. Only the first 30 frequencies are solved, and then only if the wave height power $S(\omega)$ is above some noise threshold (typically 0.01 m^2 Hz^{-1}).

The first and second moments of the directional distribution $D(\omega, \theta)$ can be used to summarize the wave directionality and resolution properties. The mean direction is calculated as the phase angle of the first complex component (a_1, b_1) of the discrete Fourier transform of the directional distribution (e.g., Allender et al. 1989), that is,

$$\theta_{\text{mean}}(\omega) = \arctan(b_1/a_1), \tag{12}$$

which is equivalent to solving the first-moment equation

$$0 = \int_{\theta_{\text{mean}}-\pi}^{\theta_{\text{mean}}+\pi} (\theta - \theta_{\text{mean}}) D(\omega, \theta)\, d\theta. \tag{13}$$

Then the directional spread is defined as the second moment of $D(\omega, \theta)$, that is,

$$\Delta\theta(\omega) = \left[\int_{\theta_{\text{mean}}-\pi}^{\theta_{\text{mean}}+\pi} (\theta - \theta_{\text{mean}})^2 D(\omega, \theta)\, d\theta\right]^{1/2}. \tag{14}$$

This directional spread parameter is quite sensitive to off-peak noise. Another measure of the directional spread is the full width half maximum (FWHM), which describes the width of the main peak, ignoring background.

A useful reference for the wave height spectrum is the well-known JONSWAP spectral form [Hasselmann et al. (1973); with constants for open Pacific Ocean taken from Chiswell and Kibblewhite (1981)]

$$S(\omega) = \alpha g^2 \omega^{-5} e^{-1.25(\omega/\omega_p)^4} \gamma^b, \tag{15}$$

where ω_p is the peak spectral frequency, $\alpha = 0.0081$, $\gamma = 1.55$, $\sigma = 0.09$, and $b = \exp[-(\omega - \omega_p)^2/2\sigma^2\omega_p^2]$. Assuming an equilibrium wind-wave field (a limiting case requiring large fetches and steady wind for long duration), we can calculate the peak frequency from $f_p = g(2\pi u_{10})^{-1}$, where u_{10} is the wind speed at a 10-m height. Also, Donelan et al. (1985) and Banner (1990) recommend for an equilibrium wind-sea, a directional spreading functional form

$$D(\theta) = \frac{1}{2}\beta \cosh^{-2}[\beta(\theta - \theta_{\text{mean}})], \tag{16}$$

with the spreading coefficient β dependent on frequency as

$$\beta = \begin{cases} 2.61\left(\dfrac{\omega}{\omega_p}\right)^{1.3}, & 0.56 < \dfrac{\omega}{\omega_p} < 0.95 \\ 2.28\left(\dfrac{\omega}{\omega_p}\right)^{-1.3}, & 0.95 < \dfrac{\omega}{\omega_p} < 1.6 \\ 10^{-0.4+0.8393\exp[-1.134\ln(\omega/\omega_p)]}, & \dfrac{\omega}{\omega_p} > 1.6 \end{cases} . \quad (17)$$

These reference height and directional spreading functions will be used in the next section to generate synthetic data and to compare with experimental results in section 5.

4. Numerical tests

Numerical wave field simulations were pursued to test various array geometries and to quantify the resolution limitations of these methods. For testing purposes, it was necessary to generate synthetic wave fields of known directional and frequency spectra. One possible method was to matrix integrate Eqs. (5) and (6), given a directional spreading function $D(\omega, \theta)$ and array geometry vector $\mathbf{\Pi}(\theta)$. Another, more computationally intensive method was to sum a large number of sinusoidal wave velocity components of varying amplitude, direction, and phase at the specified array locations. Then the cross-spectral matrices were calculated from the synthetic velocities exactly as for real data. The matrix integration method yielded idealized results, as direct matrix integration is equivalent to having an infinite frequency and directional resolution, no spectral estimation errors, and a large signal-to-noise (S/N) ratio. Discussions of resolution properties inherent to the ML and IML methods using direct matrix integration have been presented previously (e.g., Krogstad et al. 1988; Marsden and Juszko 1987; Oltman-Shay and Guza 1984; Tsanis and Brissette 1992) and were confirmed by similar tests in this context. In particular, when operating on these idealized cross-spectral matrices a dramatic improvement in directional resolution and accuracy was provided by the IML method. Also, the matrix integration method was less computationally demanding and, thus, more convenient for testing the resolution properties of various array geometries. However, more realistic tests must include the effects of cross-spectral estimation errors from finite- (40–60 min) data records and noisy velocity measurements. Thus, the sinusoidal summation method was implemented for these tests, using 60 frequencies from 0.01 to 0.6 Hz and 360 directions in a full circle. To simulate real ocean conditions, equilibrium wind-wave directional spectra of the form outlined in Eqs. (15)–(17) were used. A random noise velocity of 0.25 m s^{-1} amplitude was added to the synthetic wave velocities to include the effects of Doppler estimation uncertainty as discussed in section 2.

The first test sought to quantify the absolute resolution of the ML method using a unidirectional (plane) wave field. Using a record length of 40 × 128 pings (51 min) the ML algorithm, within the frequency range 0.05–0.34 Hz, recovered the input mean direction to ±2°, with a directional spread $\Delta\theta$ of 17.4°, and a FWHM of 6°. The $\Delta\theta$ parameter is sensitive to off-peak energy, which in this case was no larger than 0.5% of the main peak. These spread parameters can be taken as the angular resolution limits of this method, given high-quality data. At frequencies below 0.05 Hz the angular resolution (as measured with $\Delta\theta$ and FWHM) decayed badly as the wavelengths exceeded six times the maximum array aperture. Above 0.34 Hz the rapidly decreasing spectral power relative to the velocity noise level caused the ML calculation to become unstable, resulting in larger off-peak energy. It might be possible to tune the array for better angular resolution at lower frequencies by increasing the array spacing. However, the upper-frequency limit is imposed by the basic side-scan range resolution (3 m) and the velocity estimation noise threshold combined with the rapid decrease in wave amplitude at higher frequencies.

A series of unimodal spread spectrum tests suggested that this technique could reproduce, with moderate fidelity, a realistic unimodal wave field. For example, 50 × 128 synthetic pings were generated using a unimodal wave field of the form in Eq. (16) with mean direction 160° and $\beta = 2.0$, which implies a directional spread = 26° and FWHM = 54°. The ML calculation, when averaged over 0.05–0.34 Hz, yielded $\theta_{mean} = 159° \pm 6°$, $\Delta\theta = 37° \pm 5°$, and FWHM = 61° ± 7°, which were reasonably close to their reference values. Only an insignificant improvement was provided by the IML

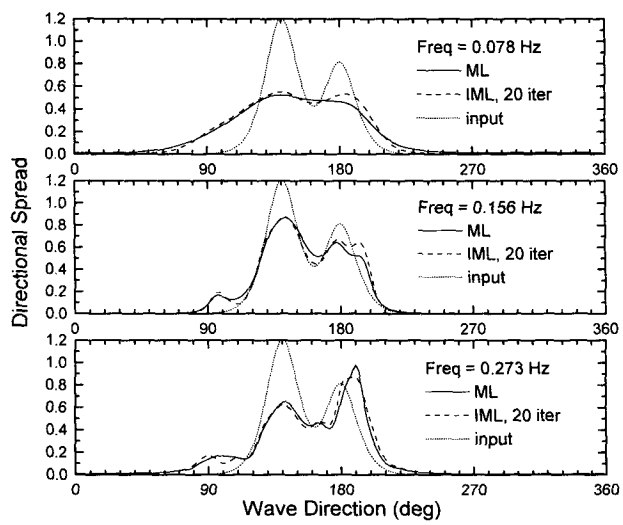

FIG. 6. Comparison of directional spreading functions $D(f, \theta)$ for ML and IML analyses of bimodal synthetic wave field data at 0.078, 0.156, and 0.273 Hz.

procedure (20 iterations), which yielded $\Delta\theta = 34° \pm 4°$ and FWHM = 60° ± 7°.

A more-demanding test is shown in Fig. 6 of the ML and IML performance in extraction of a bimodal wave field, which was a superposition of $2\beta = 4.0$ [Eq. (16)] spreading function, with 60% and 40% relative power, separated by 40°. This example used 50 × 128 synthetic pings. In general, both methods extracted the bimodal character of the input but significantly underestimated the wave power in the two peaks. Clearly, the directional resolution improved with increasing frequency. Averaged over the frequency interval 0.05–0.35 Hz, the ML result yielded a mean direction of 156° ± 3° and a directional spread of 38° ± 7° (the input values were $\theta_{mean} = 156°$ with $\Delta\theta = 23.5°$), with similar results for the IML method. Both methods produced instabilities, especially at higher frequencies, that resulted from cross-spectral estimation errors and raw velocity noise. Typically, spurious peaks were observed along the array axes (in this example at 100° and 190°). Such instabilities were not present in the idealized simulations performed using the matrix integration method (performed here and presented in many other works). From the idealized matrix integration simulations, a dramatic directional improvement was expected from the IML method, which did not occur in these simulations. In general, the IML method was unable to compensate for small errors in the input cross-spectral matrices and tended to the enhance instabilities present in the ML solution.

5. Analysis of ocean data

The SeaScan instrument platform was deployed in the northeastern Pacific Ocean near 48.8°N, 127.0°W on several occasions as part of a larger acoustic study of mixed layer processes during December 1993. Figure 7 shows the wind history for a 2.5-day period in early December. The wind speed and direction at a 3-m height, air and water temperature, and barometric pressure were measured with a meteorological buoy (Minimet), which was freely drifting within 2 km of SeaScan. Data from a real-time wind and wave climate buoy, known as MEDS LaPerouse (Canadian Government Marine Environmental Data Service) located at 48.83°N, 126.0°W (74 km east of SeaScan), were also available for comparison. The winds were dominated by the passage of two frontal systems, with especially rapid changes in wind speed and direction at the Minimet location on year-days 336.6 and 337.4. Due to the rapid (<12 h) changes in wind climate, the wind-sea components of the wave field were duration limited (i.e., not equilibrium spectra) and continually shifting in direction. Notice an approximate 12-h time lag in wind speed and directional between Minimet and MEDS LaPerouse, due to the 74-km separation, as the weather systems propagated onshore. (Air temperature pressure also showed the same distinct time lag.) This multimodal wind-wave climate makes interpretation of the directional spectral results more complicated and provides perhaps the toughest operational test for a directional spectrum measurement technique.

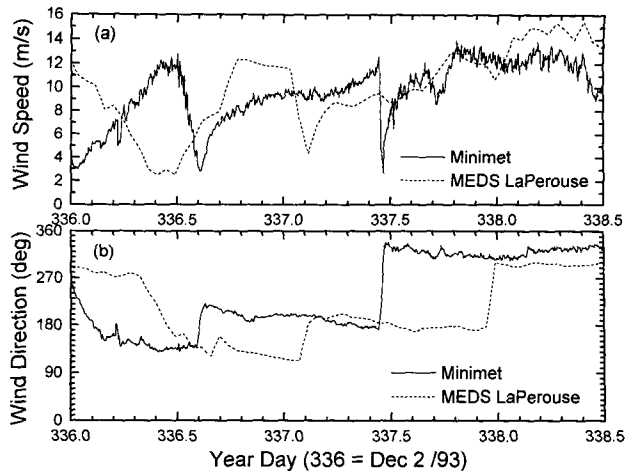

FIG. 7. Surface winds in the northeastern Pacific for 2–4 December 1993. SeaScan and Minimet buoy located near 48.8°N, 127.0°W, and MEDS LaPerouse located at 48.83°N, 126.0°W. (a) Speed at a 3-m height, (b) direction (°T).

An example dataset from SeaScan taken 1430–1530 PST 3 December will be examined in detail. At this time, the wind was slowly rising with an average (1400–1530) speed of 12 m s^{-1} (corrected to a 10-m height) from a direction of 321° ± 3°T. Note an abrupt change in wind speed, with a directional change from 180° to 325°, about 4 h before the SeaScan data period. This left insufficient time to establish an equilibrium wind-sea spectrum in the new wind direction, and significant wave energy from the old wind direction was still present. Furthermore, the local wind could be only a rough predictor of wave fields that were generated distantly by these moving storms. At this site and time, the air and water temperatures were 7.5° and 10.4°C, respectively. The side-scan beams were computer driven during this hour to maintain an x-axis heading of 249°, with the instrument platform suspended at a mean depth of 22.4 m.

As previously described, the averaged surface wave height spectrum $S(\omega)$ was calculated from the instantaneous surface elevation, with the result shown in Fig. 8. For this spectrum, the significant wave height was 4.00 m, and the peak frequency was 0.085 Hz. Two prominent *swell* peaks (frequencies 0.06–0.12 and 0.12–0.14 Hz) were present, which were the remnants of older storm events with winds of 12–15 m s^{-1}. These two swell peaks were consistent features of the SeaScan height spectra for the previous 24 h. For comparison the MEDS LaPerouse height spectrum is plotted, taken

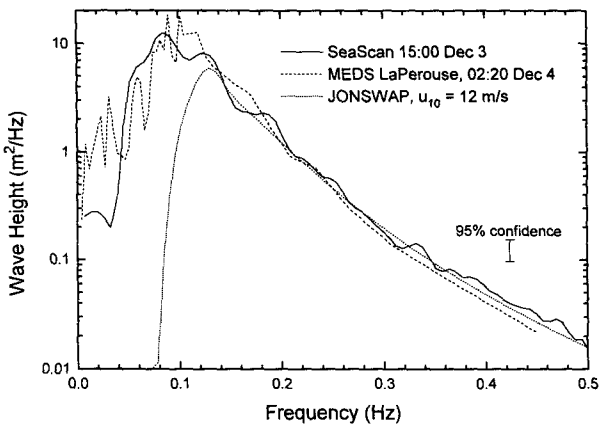

FIG. 8. Comparison of wave height vs frequency spectra. SeaScan spectrum from vertical sonars height starting 1430 PST 3 December 1993, averaged over 50 × 128 samples at 0.6 s per sample. MEDS LaPerouse spectrum from 0020 PST 4 December averaged over 34 min. Reference wind-sea spectrum from Eq. (16) using u_{10} = 12 m s^{-1}.

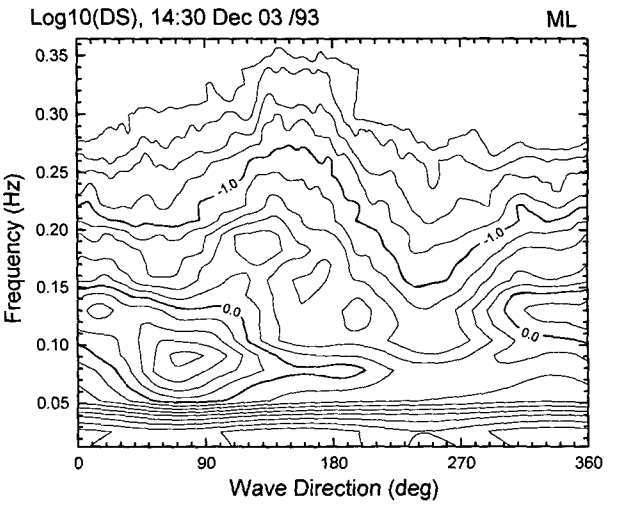

FIG. 9. The ML directional spectrum from SeaScan starting 1430 PST 3 December 1993 in the northeastern Pacific. Wind at a 10-m height was 12 m s^{-1} from 330°. Contours are $\log_{10}[G(\omega, \theta)]$ with minimum of −1.8 and increment of 0.2. Waves propagate toward direction shown.

at 0020 PST 4 December (remember the 12-h weather lag). With a 12 m s^{-1} wind speed, an equilibrium wind-wave *sea* has a peak frequency near 0.13 Hz. However the wind-sea in this case was duration limited, with an observed peak frequency at 0.18 Hz. This yielded a wave age (c_p/u_{10}) of 0.72. The dotted line shows the equilibrium wind-sea spectrum calculated from Eq. (16) using u_{10} = 12 m s^{-1}, which yields spectral levels in close agreement with the SeaScan and MEDS LaPerouse spectra over the range 0.12–0.45 Hz. The spectrum falls to a low-frequency noise level below 0.05 Hz.

Sixty-four hundred (50 × 128) samples of side-scan horizontal velocity at 16 range points along each side-scan beam were used in the calculation of directional spectrum estimates shown in Figs. 9 and 10. The contours on both figures are $\log_{10}[G(\omega, \theta)$ re 1 m^2 Hz^{-1} rad^{-1}] in increments of 0.2 with minimum contour of −1.8. Both directional spectra clearly reveal separate propagation directions for the wind-driven sea (0.18–0.35 Hz), a short-period swell (0.10–0.25 Hz), and a longer-period swell (0.06–0.25 Hz). Note that the ML spectrum clearly indicates a small directional shift (from 130° to 145°) in the wind-sea with increasing frequency. For the ML solution (Fig. 9), the peak propagation direction for the wind-sea (0.18–0.35 Hz) was 141° ± 8° with θ_{mean} of 140° ± 7°, both of which closely match the wind direction (from 321° ± 3°). The ML wind-sea directional spread was 83° with FWHM of 68°. The large values of directional spread for the wind-sea are due to significant amounts of off-peak energy, attributable to the noisy velocity cross-spectra shown in Fig. 3 and wave field multimodality. The short-period swell at 0.12–0.25 Hz was propagating toward 015° and was a consistent feature of the directional spectra throughout the 2-day deployment. The longer-period swell propagating toward 070° is the remnant of the strong southwesterly wind from year-days 336.6 to 337.4. The FWHM for these swell components were 51° and 62°, respectively. The small swell group at 0.075 Hz, 180° is another consistent peak throughout the deployment.

The peak and mean directions of the IML solution (Fig. 10) were biased slightly toward 159°, which corresponds to an array axis, with the directional spread and FWHM slightly smaller. Some smoothing of the

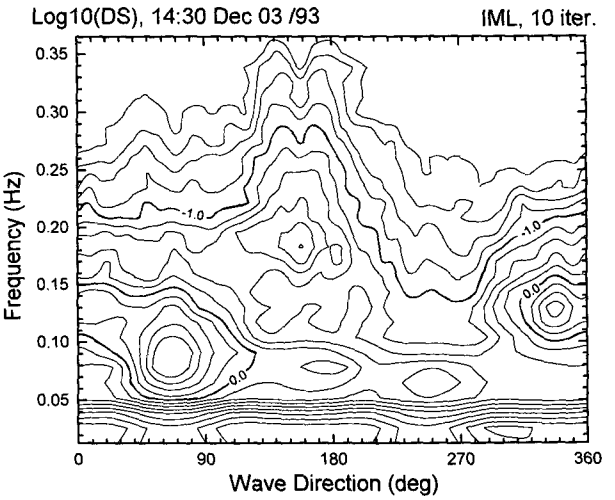

FIG. 10. Iterative ML directional spectrum (10 iterations) from same data as shown in Fig. 9 (same contour parameters).

IML spectrum [at each frequency, $D(\theta)$ were averaged over five points, or $\pm 4°$] was required to reduce small-scale directional instabilities. The wind-sea components (0.18–0.35 Hz) showed a mean direction of 146° ± 6°, a directional spread of 73° ± 6°, and a FWHM of 55° ± 7°. The two swell wave groups now have reduced directional spread with FWHM of 35° for the short swell (0.12–0.25 Hz) and 43° for the longer-period swell. Also notice that the IML spectrum more effectively separated the wind-sea (0.18–0.35 Hz, 145°) from the longer-period wave components, as seen by the decreased level of the saddle points between them. As in the numerical tests, the IML method tended to enhance slightly the instabilities present in the ML spectrum. Note the splitting of the spectral peak in the IML spectrum above 0.30 Hz at a direction of 159°, which corresponds to the x axis of the side-scan array. Slight directional instabilities of this type were also observed by Krogstad et al. (1988). Fortunately, this directional splitting has only a small effect on the bulk directional statistics.

Finally, a direct comparison at wind-sea frequencies between the ML and IML directional spread and the Donelan et al. (1985) empirical formulas is shown in Fig. 11. The figure shows the spread at 0.234 Hz, which is marginally above the two swell wave components, which cause multimodality. Note from Figs. 8, 9, and 10 that the wind-sea peak frequency was 0.18 Hz. Using this peak frequency, the reference spreading function [Eqs. (16) and (17)] uses $\beta = 1.62$ with a mean direction toward 141° (local wind direction). Hence, the reference curve has $\Delta\theta = 32°$ and FWHM = 66°. In general, the experimental results show significant wave power in the off-peak directions and, thus, less power in the peak, due to contamination from the two swell wave components and noisy cross-spectral data. The $\Delta\theta$ values for the ML and IML solutions are 82° and 69°, respectively, which are enormous compared to the reference. The IML result shows an increase in peak power over the basic ML curve at the expense of a bias toward the array axis at 159°. The IML algorithm apparently amplifies instabilities imposed by the array geometry. The FWHMs for the ML and IML curves are 72° and 56°, respectively, which are more in agreement with the reference value. Unfortunately, when operating in a multimodal, rapidly evolving wave environment such comparisons can never effectively separate measurement error from wave field multimodality.

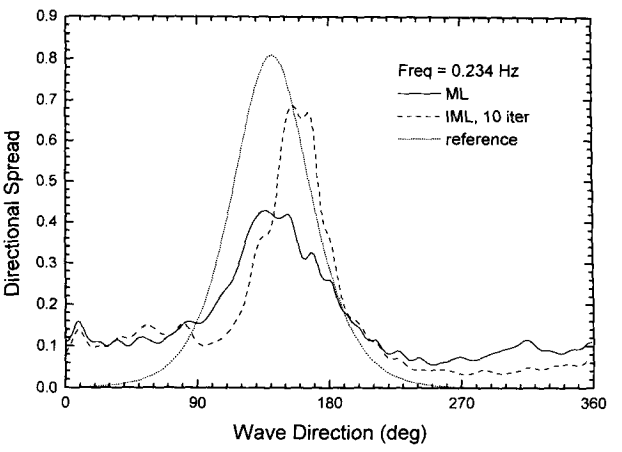

FIG. 11. Comparison of wind-driven sea directional spread at 0.234 Hz from ML and IML analysis with reference spreading function from Donelan et al. (1985), Eqs. (16) and (17).

6. Summary discussions

The estimation of Doppler velocity using 103-kHz steerable side-scans is a practical tool for the investigation of ocean surface wave spectra in the frequency range 0.05–0.35 Hz. The side-scan backscatter targets are layers or clouds of microbubbles, created by breaking waves, which are generally confined to within 3 m of the ocean surface. This microbubble injection is commonly found at wind speeds of more than 5 m s^{-1}. The theoretically predicted velocity uncertainty for the side-scan pulses used here is 14 cm s^{-1}, with an along-beam range resolution of 3.3 m. Some increase in measurement accuracy could be achieved through the use of higher acoustic frequencies (e.g., 200 or 300 kHz). However, large velocity spectral *noise* levels due to the combined effects of acoustic/electronic signal-to-noise limitations and natural microbubble variability were observed, with a minimum spectral noise threshold of 0.06 $m^2 s^{-2} Hz^{-1}$ at ranges up to 100 m. This corresponds to an effective Doppler measurement variance of 0.05 $m^2 s^{-2}$ (or a velocity uncertainty of 22 cm s^{-1}), which is considerably larger than theoretical predictions. Both Pinkel and Smith (1992) and Trevorrow and Farmer (1992) showed measured velocity variances between 1.4 and 2.0 times larger than theoretical predictions, dependent on environmental conditions. Clearly, this increased velocity estimation uncertainty will degrade any directional spectrum estimates. At ranges greater than 100 m, decreased signal levels due to spherical spreading and seawater and bubble absorption contribute to increased velocity estimation noise. At greater ranges and shallower grazing angles, increased velocity estimation errors due to wave-trough and bubble-cloud shadowing effects reduce the signal to noise of higher-frequency measurements. Deeper bubble plumes cause a depth integration of horizontal wave velocity, resulting in a reduction of measured velocity from the surface value, which is significant at higher frequencies. Overall, the natural bubble cloud variability, combined with acoustic/electronic signal-to-noise limitations and the rapid decrease in wave velocity power at higher frequencies ($\sim f^{-3}$), limits the measurement of ocean wave velocity spectra to below

0.35 Hz at horizontal ranges less than 150 m, or less than 0.25 Hz at ranges up to 200 m.

For freely drifting platforms, the residual orbital motions due to long-period ocean waves can be significant, requiring corrections to measured wave height and horizontal velocity. For this task it is imperative to measure the full three-dimensional platform motion, using for example three-axis accelerometers. For the SeaScan platform deployed at a 22.4-m depth with a significant wave height of 4.0 m, the rms vertical displacement was 0.41 m, and the rms vertical velocity was 0.20 m s^{-1}. At short ranges, the side-scan beam grazing angle is nonzero, allowing contamination of the measured horizontal wave velocities by both vertical wave velocity and vertical platform motions. These geometric effects are readily incorporated into the data processing. Additionally, the horizontal platform motion (coupled to the vertical) also contaminates the velocity measurements along the side-scan beams. Unfortunately, the horizontal platform motion was not directly measured and had to be extracted from the range-averaged velocity components along each side-scan beam. This further required a scheme to remove long-period wave velocity versus range variations along each side-scan beam. Surface drift currents due to wind and tide (where present) can be estimated from the time and range-averaged horizontal velocity along each beam.

Using two side-scan beams steered in an earth-fixed coordinate system, a method has been found to extract the directional spectrum using maximum-likelihood array processing methods. In this scheme, 16 array point at 6.1-m intervals from 25 to 123 m in horizontal range along two orthogonal directions were used, but a great deal of flexibility in array spacing is possible. This method is also easily extended to include more than two side-scan beams, which would greatly enhance the directional spectral results. A minimum of about 50 min of velocity data has been found necessary to properly estimate the cross-spectral matrices between the measurement points. The ML method has moderate angular resolution, which approaches 6° (FWHM) with a minimum $\Delta\theta$ of 17° in the frequency range 0.05–0.35 Hz. On the basis of numerical tests on synthetic velocities, the directional accuracy in peak and mean directions is ±5° to ±8°. This range of angular resolution is consistent with results reported in Krogstad et al. (1988) but extend to slightly higher frequencies. Numerical simulations suggest that this method can recover with moderate distortion both unimodal and bimodal, directionally spread wave fields.

Tests using real ocean data confirm that this ML array method can recover believable wind-sea and swell directional spectra, in spite of the relatively poor data quality. For the northeastern Pacific data, the ML solutions extracted a mean propagation direction for the wind-sea (0.18–0.35 Hz) aligned within a few degrees of the wind direction. Measured height spectra from the SeaScan platform agreed well with independent spectral estimates from a surface buoy and reference height spectra for equilibrium wind-seas [Eq. (15)]. The average directional spread $\Delta\theta$ of a typical wind sea was determined to be 83° for the ML method and 73° for the iterative ML method, which were both much larger than the expected 34° from reference spreading functions [Donelan et al. 1985, Eqs. (16) and (17)]. This large discrepancy was directly attributable to the relatively large velocity cross-spectral variability (explained above), to which the $\Delta\theta$ measure is particularly sensitive. The FWHM and directional shape of the wind-sea components were in much better agreement with the reference. This result suggests caution in using directional spreads from higher-frequency wind seas.

When operating on nonideal, noisy cross-spectral data, the IML method does not deliver drastically improved accuracy, as a priori expected from previous, idealized simulations. Array geometric limitations, spectral estimation errors, and noisy velocity measurements produce instabilities in the cross-spectral matrices, which are enhanced by the IML calculations. Real ocean results showed only modest directional resolution improvement over the ML result, at the expense of a bias toward array axis directions. Without a dramatic improvement in velocity data quality, the IML method implemented here should not be used.

These directional spectral methods can also be applied to data from side-scan instruments that are subsurface moored, fixed to larger structures (e.g., oil platforms), or bottom mounted. For fixed installations where power and recording capacity are not an issue, improved directional performance would be gained by using more than two side-scan beams. Also, in such cases the platform motions would be much reduced or absent. However, in shallow waters the effects of tides and bottom reverberation are generally more pronounced. Shallow-water and surface current corrections to the surface wave dispersion relation may be required.

Acknowledgments. The author is indebted to Dr. David Farmer and his sponsors for the opportunity and encouragement to pursue this work. The instrumentation and experimental developments were funded by Grants from the Office of Naval Research. Support for the author was derived from the Canadian Interdepartmental Panel on Energy Resource Development. The author also wishes to recognize the tireless efforts of Alan Adrian, Craig Elder, Ron Teichrob, and Kim Wallace for the electronic and mechanical development of SeaScan.

REFERENCES

Allender, J., T. Audunson, S. Barstow, S. Bjerken, H. Krogstad, P. Steinbakke, L. Vartdal, L. Borgman, and C. Graham, 1989: The

WADIC project: A comprehensive field evaluation of directional wave instrumentation. *Ocean Eng.*, **16,** 505–536.

Banner, M., 1990: Equilibrium spectra of wind waves. *J. Phys. Oceanogr.*, **20,** 966–984.

Brumley, B., R. Cabrera, K. Deines, and E. Terray, 1991: Performance of a broad-band acoustic Doppler current profiler. *IEEE J. Oceanic Eng.*, **16,** 402–407.

Chiswell, S., and A. Kibblewhite, 1981: Spectra of the fully developed wind-generated ocean wave field west of central New Zealand. *N. Z. J. Mar. Freshwater Res.*, **15,** 81–84.

Crawford, G., and D. M. Farmer, 1987: On the spatial distribution of ocean bubbles. *J. Geophys. Res.*, **92**(C8), 8231–8243.

Davis, R., and L. Regier, 1977: Methods for estimating directional wave spectra from multi-element arrays. *J. Mar. Res.*, **35,** 453–477.

Donelan, M., J. Hamilton, and W. Hui, 1985: Directional spectra of wind-generated waves. *Phil. Trans. Roy. Soc. London, Ser. A,* **315,** 509–562.

Farmer, D. M., and S. Vagle, 1989: Waveguide propagation of ambient sound in the ocean-surface bubble layer. *J. Acoust. Soc. Amer.*, **86,** 1897–1908.

Hasselmann, K., and Coauthors, 1973: Measurements of wind-wave growth and swell decay during the Joint North Sea Wave Project (JONSWAP). *Dtsch. Hydrogr. Z.*, **A12**(Suppl.), 95 pp.

Herbers, T., and R. Guza, 1990: Estimation of directional wave spectra from multicomponent observations. *J. Phys. Oceanogr.*, **20,** 1703–1724.

——, R. Lowe, and R. Guza, 1991: Field verification of acoustic Doppler surface gravity wave measurements. *J. Geophys. Res.*, **96**(C9), 17 023–17 035.

Krogstad, H., R. Gordon, and M. Miller, 1988: High-resolution directional wave spectra from horizontally mounted acoustic Doppler current meters. *J. Atmos. Oceanic Technol.*, **5,** 340–352.

Long, R., and K. Hasselmann, 1979: A variational technique for extracting directional spectra from multi-component wave data. *J. Phys. Oceanogr.*, **9,** 373–381.

Longuet-Higgins, M., D. Cartwright, and N. Smith, 1963: Observations of the directional spectra of sea waves using the motion of a floating buoy. *Ocean Wave Spectra,* Prentice-Hall, 111–136.

Lygre, A., and H. Krogstad, 1986: Maximum entropy estimation of the directional distribution in ocean wave spectra. *J. Phys. Oceanogr.*, **16,** 2052–2060.

Marsden, R., and B. Juszko, 1987: An eigenvector method for the calculation of directional spectra from heave, pitch, and roll buoy data. *J. Phys. Oceanogr.*, **17,** 2157–2167.

Miller, K., and M. Rochwarger, 1972: A covariance approach to spectral moment estimation. *IEEE Trans. Inf. Theory,* **IT-18,** 588–596.

Oltman-Shay, J., and R. Guza, 1984: A data-adaptive ocean wave directional-spectrum estimator for pitch and roll type measurements. *J. Phys. Oceanogr.*, **14,** 1800–1810.

Pawka, S., 1983: Island shadows in wave directional spectra. *J. Geophys. Res.*, **88**(C4), 2579–2591.

Pinkel, R., and J. Smith, 1987: Open ocean surface wave measurement using Doppler sonar. *J. Geophys. Res.*, **92**(C12), 12 967–12 973.

——, and ——, 1992: Repeat sequence coding for improved precision of Doppler sonar and sodars. *J. Atmos. Oceanic Technol.*, **9,** 149–163.

Smith, J., 1989: Doppler sonar and surface waves: Range and resolution. *J. Atmos. Oceanic Technol.*, **6,** 680–696.

——, and R. Pinkel, 1991: Improvement of Doppler estimation through repeat sequence coding. *Proc. Oceans '91,* Honolulu, HI, Institute of Electrical and Electronics Engineers, 977–984.

——, and G. Bullard, 1995: Directional surface wave estimates from Doppler sonar data. *J. Atmos. Oceanic Technol.*, **12,** 617–632.

Thorpe, S. A., 1982: On the clouds of bubbles formed by breaking wind-waves in deep water, and their role in air–sea gas transfer. *Phil. Trans. R. Soc. London, Ser. A,* **304,** 155–210.

Trevorrow, M. V., and D. M. Farmer, 1992: The use of Barker codes in Doppler sonar measurements. *J. Atmos. Oceanic Technol.*, **9,** 699–704.

——, and R. Teichrob, 1994: Self-contained acoustics platforms for probing ocean surface processes. *IEEE J. Oceanic Eng.*, **19,** 483–492.

Tsanis, I., and F. Brissette, 1992: Wave directional spectra measurements by small arrays in Lake Ontario. *J. Great Lakes Res.*, **18,** 489–506.

Zedel, L., 1994: Deep ocean wave measurements using a vertically oriented sonar. *J. Atmos. Oceanic Technol.*, **11,** 182–191.